

Visual Computing of Dissected Aortae*

Antonio Pepe^{a,b,c,*}, Dominik Fleischmann^a, Dieter Schmalstieg^b, Jan Egger^{b,c}

^a*Stanford University, School of Medicine, Department of Radiology, Cardiovascular
Imaging Division, 300 Pasteur Drive, Palo Alto, CA 94304, USA*

^b*Graz University of Technology, Institute of Computer Graphics and Vision, Inffeldgasse
16, 8010, Graz, Austria*

^c*Computer Algorithms for Medicine Laboratory, Graz, Austria*



*Technical Report for the Marshall Plan Foundation

*Corresponding author

Email addresses: antonio.pepe@tugraz.at, apepe@stanford.edu (Antonio Pepe),
d.fleischmann@stanford.edu (Dominik Fleischmann), schmalstieg@tugraz.at (Dieter
Schmalstieg), egger@tugraz.at (Jan Egger)

URL: <http://studierfenster.tugraz.at/> (Antonio Pepe)

Abstract

Aortic disease is a broad term which includes aortic aneurysms, dissections, intramural hematoma and other conditions. The management of these conditions varies from long-term pharmacological treatment to immediate aortic surgery. Although different decisions can be made on specific cases, surgical intervention is advised for patients with an aortic diameter larger than 5.50 cm. These diameters are often not always measured at regular positions, due to different medical approaches. Recent work has suggested eleven specific points along the aorta where to measure the aortic diameters; but the view angle as well as exact delineation of the diameter are subject to the user's image understanding. In this work, we define and validate a deep learning method to automatically retrieve this information in a standardized fashion. Furthermore, we suggest an approach which, for each of these points, provides an estimation of the original diameter before the onset of the disease. The method is executed in three following steps, i) a convolutional neural network segments the aorta, ii) a second deep neural network detects the location of the eleven points, iii) a third neural network reconstructs the original shape of the aorta, which can be used for growth estimation. The resulting measurements are compared with those obtained from different experts. Furthermore, some of the algorithms here discussed have been made available on the public open science platform Studierfenster (<http://studierfenster.tugraz.at/>).

Keywords: Aortic Dissection, Image Segmentation, Landmark Detection, Deep Learning, Centerline, Shape Completion



Marshallplan-Jubiläumsstiftung
Austrian Marshall Plan Foundation
Fostering Transatlantic Excellence

AORTIC DISSECTION

MECHANICS - MODELING - SIMULATION



1. Introduction

Aortic pathologies, such as aortic aneurysms, dissections, and penetrating ulcers are critical conditions, which, in addition to medical treatment or surgery, require life-long follow-up examinations [1]. During these examinations, 3D imaging data of the patient are acquired using contrast-enhanced computed tomography angiography (CTA) or other imaging modalities [1]. The acquired images are used to measure the maximum major- and minor-axis diameters of the aortic lumen in a standardized plane orthogonal to the vessel (see Figure 1, red lines) [2]. In the clinical practice, the orthogonal planes are usually manually fitted by trained users using double-oblique reformations [3]. This can result in time-consuming operations and a user-dependent random error, due to a different image perception.

Centerline-based approaches have been suggested to automate this task and automatically measure the diameters in the thoracic aorta [4]. These methods have been shown to be ready for clinical use when tested on images of healthy aortae [4]. Nonetheless, the extraction of a centerline requires a segmentation of the blood vessel [4, 5, 6]. Previous work has shown that conventional approaches might not be suitable for the segmentation of the aorta in the presence of critical conditions such as aortic aneurysms or dissections, especially if they are in a stage of thrombosis [5]. In this work, we reduce the current clinical limitations by suggesting an automatic approach for the segmentation of aortae in CTA images; with a specific focus on dissected aortae. Furthermore, we suggest a standardized and automatic approach for the localization of the relevant positions where to measure the aortic diameters. Finally, we provide a way to measure these diameters and compare them with the a predicted, pre-disease size.

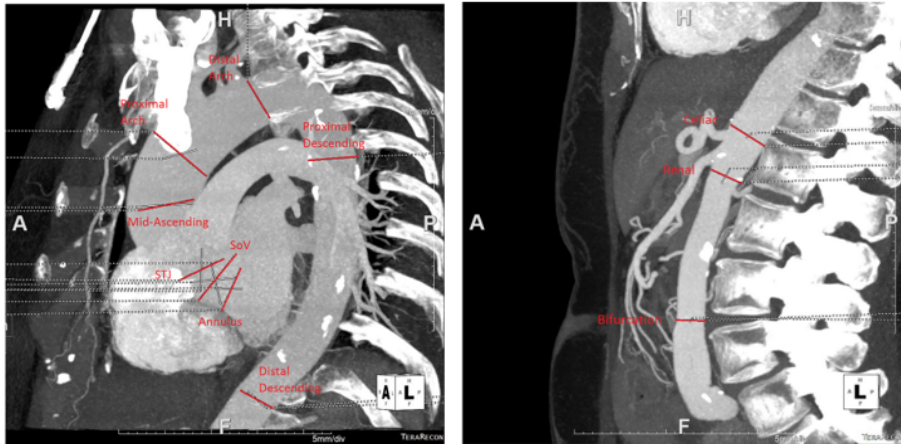


Figure 1: Visualization of the of the aortic measurements (diameters) along the orthogonal plane at specific locations, the so-called 11 aortic landmarks. (Image courtesy of Virginia Hinostroza, Stanford University).

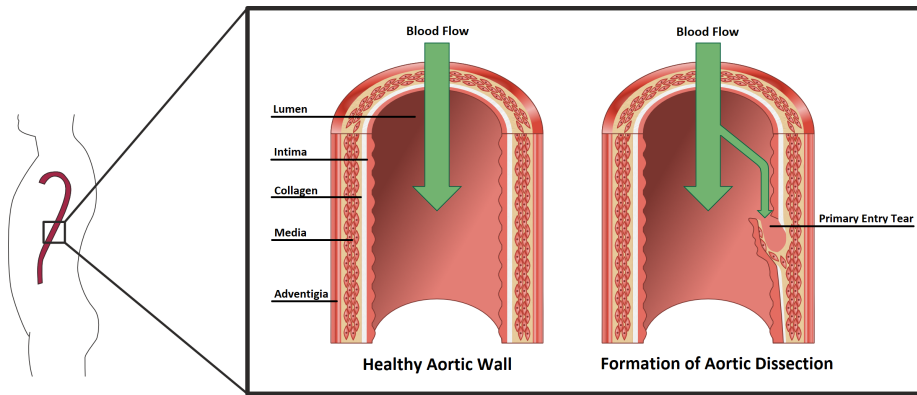


Figure 2: Simplified visualization of the aortic wall, with the microstructure of the three layers – intima, media, and adventigia – interconnected with collagen fibers [7] (left). Formation of the primary entry tear (right).

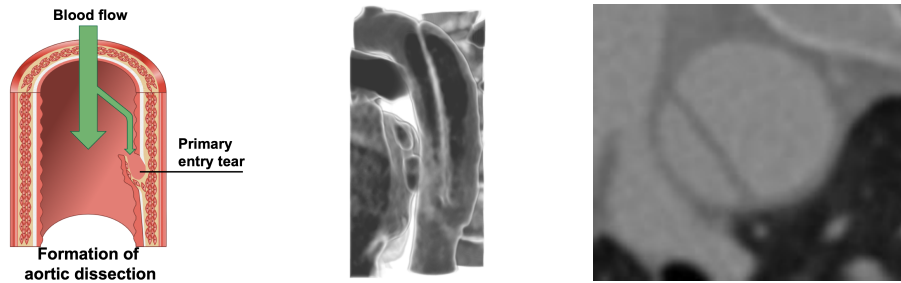


Figure 3: Illustration of an aortic dissection (AD). In color: The formation of a false lumen (FL). In gray: actual CTA images of AD.

2. Medical Background

The aortic dissection (AD) is an uncommon, but life-threatening condition of the aorta (Figure 2 and Figure 3), caused by a diseased medial layer inside the aortic wall [8, 9]. The wall of the aorta is characterized by three separate layers – intima, media, and adventigia – which are interconnected by means of collagen fibers (Figure 2) [10]. Characteristic is the sudden development of a so-called *primary entry tear*, a defect on the luminal side of the aorta [10]. This allows blood to enter the teared aortic wall, further dissect it, and form a new ‘false’ blood flow channel inside the aortic wall. As the dissected aortic wall is thinner and of lower mechanical strength, it may rupture, leading to a typically lethal event [9]. When the newly formed blood channel reconnects with the original ‘true’ blood flow channel of the aorta, two separate flow channels are generated, referred to as true lumen (TL) and false lumen (FL), as the interior of a blood vessel is called *lumen*. Diagnosing ADs is typically done by acquiring CTA that provides detailed anatomic information of thera-

apeutically relevant features, such as the anatomy of TL and FL. Once AD has been diagnosed, patients undergo life-long surveillance, comprising CTA scans after three months, six months and annually thereafter to monitor the progression of the aortic growth. A personalized and precise management of aortic dissection has been increasingly desired in thoracic endovascular aortic repair (TEVAR) [11]. Such a scheme can be involved in all stages of AD management, including preoperative planning, follow-up, prognosis and prediction of the long-term outcome [12]. During surgical planning, it is crucial to select and place the stent-graft based on the geometrical characteristics of the patient’s aorta, such as diameters, volumetric shape and exact location of the intimal tear [13, 14] – information which has proven to be effective in reducing complication and recurrence rates [15, 16, 17, 18]. Although not yet standardized, a crucial reason for these *patient-specific* stent-grafts is to prevent so-called ‘endoleaks’ [19, 20], and therefore, avoid a re-intervention due to a disconnection between the stent-graft and the aortic wall [21].

During follow-up, an evaluation of the dissection development is required for vascular surgeons to assess the effect of TEVAR on the patient, which includes observing the changes in diameter, volume and morphology of true and false lumina [22, 23, 24, 25]. These geometrical characteristics of aortic dissections are important prognostic factors, also in AD management. Aided by commercial software, such as Aquarius (<https://www.terarecon.com/>, TeraRecon, Foster City, CA) and 3Mensio (<https://www.3mensio.com/>), vascular surgeons can obtain a 3D model of the dissected aorta for morphological evaluation, manually segment (identify) true lumen and false lumen for diameter and volume measurement and locate the intimal tear by examining the computed tomography angiography image in a slice-wise manner [26]. Although commercial applications support surgeons and radiologists covering these tasks, they still require an intense user interaction, which results in time-consuming and error-prone operations, with a remarkable user dependability. It remains to be a challenging, time-consuming and experience-dependent task to obtain these crucial information accurately. Furthermore, investigating the onset of the disease remains rather unexplored, since acquiring data before the diagnosis of AD is highly unlikely.

3. Technical background

3.1. Deep Learning

Deep Learning is a machine-learning technique, which currently finds a wide range of different applications from the identification of objects in images, to the transformation of speech into text, and the matching of diverse data with a user’s interests for profiling and recommendations. Deep learning methods are used to transform the representation of raw data at one level to a representation at a higher, more abstract level, called latent space. Convolutional Neural Networks (CNNs) use multiple processing layers to learn representations of data with multiple levels of abstraction. Thus, CNNs have the ability to process

multidimensional array data, such as colour images, which are represented by three bidimensional arrays, containing the pixel intensities of the three colour channels.

For instance, to build an image classifier that can identify different classes (e.g. houses, planes, cars, etc.), correctly labelled training data sets are necessary. During the training phase, the network is ‘shown’ an image, and then produces an output of different scores. This represents the probability of the image to belong to a certain class/category. The main task of the network is then to allocate the correct class to an image. Thus, the correct class should have the highest probability. For this, an error function is introduced, which measures the deviation between the predicted and true classification scores. The parameters of the networks, referred to as weights, are then iteratively updated. After a training is finished, a separate test data set is used to measure the performance of the network. This last phase of testing and evaluation provides an indication of the generalization capability of a neural network to produce useful outputs on new inputs, which have not been seen during training [27]. Four specific layers are described in the following passages.

3.2. *Studierfenster*

Studierfenster is a client/server based online environment, which can be directly used in a web browser, meaning there is no need to install any further local software. The utilities provided by Studierfenster include a possibility to export and convert DICOM files, calculate the Hausdorff distance and the Dice coefficient, perform 3D face reconstructions and use a medical 3D viewer, which allows different functionalities for medical use cases [28, 29]. The tool has been initially developed by a team at Graz University of Technology [28]. In this work, we use Studierfenster for the deployment of the neural networks and visualization purposes. The software development kit has been provided by the group and will be soon released to the public.

3.3. *PyTorch*

PyTorch is a machine learning library developed by the Facebook Artificial Intelligence research group. It is currently available for Python and C++ and is a free and open-source software. All the convolutional neural networks described in this work have been implemented and trained using Pytorch version 1.3.0.

4. Contribution

In this work, we extend the state of the art in clinical management of aortic dissection with the introduction of an automatic protocol for aortic surveillance. In particular, we:

- suggest an automatic approach for the segmentation of dissected aortae based on residual deep networks and compare it with a state of the art approach;

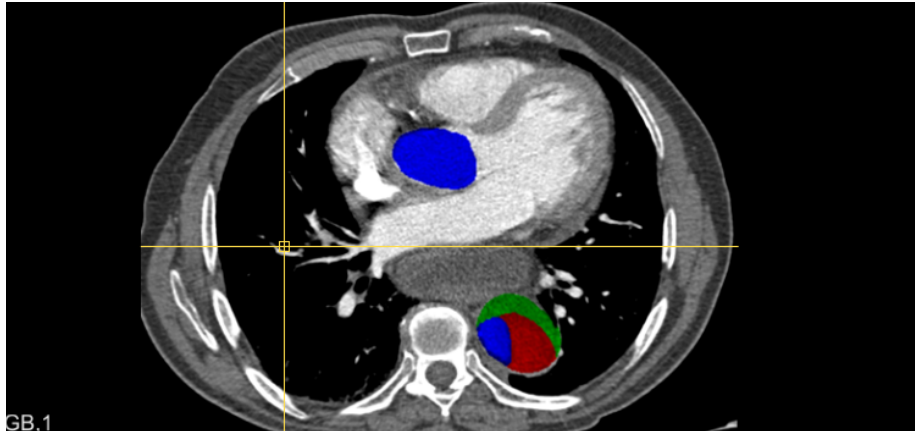


Figure 4: Visualization of a manually labelled image. In blue is depicted the label of the true lumen, in red and in green the false lumen. The green-labelled area of the false lumen depicts the formation of thrombus.

- identify landmarks of interest for surveillance protocol based on literature search and on the clinical experience of a group of radiologists and technologists;
- suggest an approach for the automatic localization of such landmarks using a heatmap regression method;
- define an image restoration network for the regression of disease in the surrounding of the landmark positions, to provide an approximation of the aortic enlargement;
- suggest a method to measure the aortic diameter, which is robust to the morphological changes introduced by the AD.

5. Imaging Data

Independent CT collections are used to train and evaluate the different algorithms explained in this work. The segmentation algorithm has been trained on the datasets provided by Higashigaito et al. [30]. The collection consists of 235 CTA scans from 47 different AD patients who underwent follow-up examinations for a median time of 4 years. For each scan, the collection includes ground-truth labels of true lumen, false lumen and thrombus; if any. An example of these labels is shown in Figure 4. Each image has been manually labelled by one out of three radiologists; in some cases the images have been refined by a second radiologist.

For the detection of the aortic landmarks, a separate image collection of 161 CTA scans from 146 different patients has been collected. For each scan, an

experienced radiology technologist has measured the major and minor aortic diameters at clinically-relevant locations in so-called double-oblique views. In this work, we refer to aortic landmark as the intersecting point between the two diameters. Each scan has been processed by one out of eleven experts; the expert’s identifier, the diameters, the landmarks and the direction of the normal planes have been saved for training and evaluation as further discussed in this work.

Additionally, since before-AD/with-AD image pairs are unavailable, we use public datasets of healthy aortae for the training of the shape reconstruction network. A total of 75 CTA datasets were acquired, 40 from the CAD-PE challenge (www.cad-pe.org) and 35 from Masoudi et al. [31].

6. Segmentation of Dissected Aortae

While a large number of studies have focused on computer-aided segmentation of the aorta [32], the segmentation of dissected aortae, including true lumen, false lumen, intimal flap and dissected wall, has been less intensively investigated, despite the strong clinical relevance. The unavailability of public datasets of aortic dissections might represent a major factor on this. For the segmentation of healthy aortae, the methodologies range from established image processing techniques such as level-set [33, 34], region-growing [35, 34] and model based approaches [36, 37, 38, 39], to emerging approaches; machine learning [40] and deep convolutional neural networks [41, 42]. The segmentation of dissected aortae, even without a semantic distinction of true and false lumina, has proven to be a more challenging task than the segmentation of healthy aortae due to the presence of the dissection membrane, unpredictable shape changes, and intensity attenuation in the false lumen [43]. This section first provides an overview of the state of the art in AD segmentation and then suggests a new approach which extends the current state of the art.

6.1. State of the art

In 2006, Kovács et al. introduced a computer-aided diagnosis system that can segment the aorta, detect the dissection membrane and identify true and false lumina successively and fully automatically [44, 45]. Utilizing the prior knowledge of the circular shape of the aorta and the Hough transform, the authors could segment the dissected aorta, regardless of the dissection membrane and the inhomogeneous distribution of the contrast agent in the false lumen. The segmented aorta is further refined using an elastically deformable model (DM); the seed points for the DM can be initialized either manually or automatically based on the anatomical prior information regarding the shape of the aortic arch. The proposed approach was evaluated on 21 3D CTA images of healthy aortae, dissected aortae and other pathological aortae, including cases of aneurysm, stenosis and stent grafting. It is foreseeable that, also according to the authors’ considerations, the approach fails on some cases of aortic aneurysm and stenosis, as the approach strongly relies on the prior information. It presents limitations

when segmenting aortae with strong variations of the diameter length. For validation, a ground truth segmentation was obtained manually and an average distance is used to quantify the segmentation performance of the system. The average time per case was six minutes on a standard PC, which is considerably faster than a manual segmentation but, at the same time, still cannot meet the requirement for time-demanding clinical applications. Then, the dissection membrane is detected within the segmented and straightened aorta by adopting Descoteaux’s sheetness measure [46] and the Hessian matrix. The dissection membrane detection is dependent on the aorta segmentation for the creation of a region of interest, therefore, it fails on aneurysmatic aortae. For the proposed design, the approach also fails on highly folded membranes where more than two aortic lumina are visible, since it relies on a specific prior model of the membrane. Finally, Kovács describes in his doctoral thesis [47], how true and false lumen can be identified and segmented following the described steps. For type-B aortic dissection (TBAD), true lumen and false lumen can be distinguished based on the a-priori assumption that the true lumen is connected to the undissected ascending aorta. For type-A aortic dissection (TAAD), the cross-sectional area is used as indicator to discriminate between true lumen and false lumen, based on the a-priori assumption that the false lumen has a larger cross-sectional area compared to the true lumen in TAAD. These operations are performed in a multiplanar reformatted space; after the identification of the two lumina, the straightened true and false lumina are transformed back into the original coordinate system. The back-transformation process can cause errors, especially in highly curved areas such as the aortic arch. To summarize, Kovács et al. proposed a fully automatic method to segment the true and false lumina. They achieved this goal with three successive steps: segmentation of the aorta, detection of the dissection membrane and identification of the two lumina. Each step is highly dependent on the preceding steps and the model-based approach exploited, to a large extent, the a-priori assumption of the morphology and properties of aortic dissection in CTA images, which made the approach liable to fail on irregularly-shaped aortae, such as aortae with aneurysms and heavy stenosis. Another model-based approach to identify and segment true lumen and false lumen is provided by Fetnaci et al. [48], who propose a modified deformable model. In particular, the authors have adapted the speed terms of the fast-marching method to obtain separated lumina. Lee et al. [49] introduced an approach, which combines multi-scale Wavelet analysis and generative-discriminative model matching to discriminate and segment true lumen and false lumen. First, the complete boundary of the aorta was detected using a semi-automatic method, which was proposed by Tek et al. [50]. Second, wavelet-analysis was used to detect edges within the dissected aorta. In this step, the edges separating true lumen and false lumen were also detected. Third, the detected edges were refined using discriminative learning and only the lumen edge points were predicted. Fourth, generative learning was used to discriminate true lumen and false lumen by estimating the density distribution within the boundary of the aorta. While deep convolutional neural networks (CNNs) are playing an increasingly important role and achieving state-of-the-

art results on many medical image segmentation tasks [51, 52, 53, 54, 55], the application of CNNs in the segmentation of aortic dissections has been under-investigated. Ziyang Li et al. used two 2D cascade convolutional networks to extract the contours of both the aorta and its true lumen respectively [56]. [57], instead, used two 3D segmentation networks, i.e., the first network was used to segment the whole aorta while the second was used to segment true lumen and false lumen simultaneously. Restricted by computational resources, both of the two studies reported a down-sampled CT image as the input of the network. Ziyang et al. [56] down-sampled the slices from 512×512 to 144×144 and Long et al. [57] down-sampled the volume to $128 \times 128 \times 256$ voxels. The two studies used the Dice Similarity Score (DSC) as comparison metric. The average DSC for [56] was 0.989 for the whole aorta and 0.925 for the true lumen on a five-fold cross-validation on 45 CT volumes. No test set and test results are provided. Long et al. [57] used 246 CTA scans for training and 30 for testing; the testing results were 0.93, 0.93, and 0.91 for the whole aorta, true lumen and false lumen, respectively. The authors also reported a three-fold average validation DSC of 0.93, 0.92 and 0.91 for 30 randomly selected CTA scans from the training set. The reported training time is 71 hours (21h for the *adventitia network* and 50h for the *intima network*) on a GPU NVidia GTX 1080 Ti for Ziyang et al. [56] while Long et al. [57] did not report this information. The latter reported an average inference time of 31.06 seconds including down-sampling (6.68 seconds), inference (6.28 seconds) and post-processing (18.1 seconds). However, it is difficult to directly compare the performance of the two approaches since different, non-public data sets have been used in each study. The output of the proposed segmentation network by Ziyang et al. [56] consists of 2D contour points of a slice. The 3D lumen mesh model of the whole aorta lumen and the true lumen can be obtained by triangulating the contour points of the adjacent slices. For the network by Long et al [57], the output is directly the 3D volume of the whole aorta, true lumen and false lumen.

6.1.1. Suggested methods

Convolutional neural networks have shown to be a promising technique for the segmentation of AD [56, 57]. Nonetheless, the suggested approaches have shown substantial limitations for AD segmentation. In this section, a hybrid approach is discussed, which covers some of the limitations presented by the discussed approaches. In particular, two approaches are hereby presented:

1. A two-step method, which initially segments the overall aortic lumen in CTA images, performs a curved planar reformation (CPR) based on the centerline of the segmented lumen, and finally performs a more accurate 3D segmentation in the CPR space, distinguishing between TL and FL;
2. A one-step method, where the two lumina, TL and FL, are segmented in a slab-based manner; casualties like mislabeling are then removed using overlapping slabs.

In the first approach, we train a residual 2D network based on CE-Net [58] (Figure 5). During this training, the labels are unified under one category, ‘aortic

lumen’. This segmentation allows to retrieve the centerline of the vessel using a distance transform [59]; and reform the image to obtain a straightened visualization of the aorta using curved planar reformation [60]. This allows to precisely crop the volume around the dissected aorta and to feed a further convolutional neural network with minimal 3D patches. In the second stage a 3D Residual U-Net [61] (??) is used to more accurately segmented the reformed volume. This 3D residual network is characterized by the presence of long and short skip connections. The short residual connections are used to build up the residual blocks and the long residual connections are used to propagate local spatial information from the encoding to the decoding path. The residual connections are obtained using sum operations whose linearity allows to efficiently propagate the information during the training process. In this second stage, the network is trained on a multi-label setting where different classes are used for TL and FL, using augmentation strategies like rotation and scaling to increase the generalization and robustness of the trained network. It is meaningful to state that the curved planar reformation is usually not a bijective transformation [60]; the so-defined neural network will be able to correctly segment the vascular structure and therefore provide a reliable volumetric measure of the disease progression. Nonetheless, technical applications such as 3D printing of physical simulation might require to obtain the segmentation of the aorta in its original shape. As alternative approach we propose here the use of a 3D Residual U-Net directly on slabs of the original volumes down-sampled by a factor of two. The usage of a 3D network allows to segment the volume with a certain understanding of the luminal class; nonetheless, by using overlapping slabs, mislabelled segmentations can be corrected by controlling the overlapping labels from the slab in the previous or following iterations. A simple and naive correction criterium is given by forcing overlapping voxels to belong to the same label and to expand this to the non-overlapping slices.

6.2. Comparison

We trained both the approaches on a training set of 140 CTA volumes from a set of 40 different patients. The test is performed on further 34 CTA volumes from a second set of 7 further AD patients. Table 1 shows the training and validation results of both approaches. First we trained the CE-Net-based network on slabs of three slices down-sampled to an axial size of 256x256 pixels. As the original network architecture uses 2D convolutional operations on 3-channel images, we use the information of the two adjacent slices to infer also a minimal spacial information to the 2D output. Using the centerline of this segmentation we resampled the volume with a fixed overall pace of 1000 slices per volume and crop the resampled slices to a size of 128x128 pixels centered to the aortic centerline. The second network based on the residual 3D U-Net is trained on slabs of 32 reformed slices. To understand the benefit of this approach, we trained the 3D network also directly on the original volumes down-sampled by a factor of two. Each training sample had an overall size of 256x256x8 voxels. All the networks have been trained using *early stop* as termination strategy. The network is directly trained to segment both the labels, TL

Table 1: Quantitative results of the segmentation network trained and validated on CTA images of AD.

Image Type	Number of Labels	Training Loss	Validation Loss
Reformed image	2	0.002	0.005
Full image	2	0.005	0.009



Figure 5: Example of segmentation on the reformed volume: CT) reformed slice, GT) ground truth image, PRED) network prediction. In grey, the true lumen; in white, the false lumen.

and FL. It can be seen how splitting the training in two phases provides more accurate results also visibly; without substantially increasing the computational requirements. Nonetheless, the transformation used to obtain the warping of the reformed vessel is not bijective. Therefore, the two-step method can not be used to reconstruct the original aortic shape without resampling artifacts due to aliasing. A possible naive solution can be obtained by resampling the volume with sufficient resolution. This results in sampling planar reformation along the centerline with a small and adaptive pace. In particular the pace is a function of the centerline curvature and of the desired resolution for the reconstruction. A too high sampling factor can result in reprocessing the same voxels multiple times, a too low sampling factor may skip significative voxels which would in turn create artifacts during the resampling of the reformed volume and reconstruction of the original shape. An alternative approach is provided by the second method where a 3D residual network is trained to segment slabs with a fixed length. In both cases a possible mislabeling of TL and FL can be fixed using overlapping slabs; in particular, to also guarantee smoothness, we used an overlap of fifty percent. Although it provides a lower accuracy, the single-step method appear to be more accurate for the generation of 3D meshes; whereas clinical application such as the measurement of the aortic diameters could benefit from the higher accuracy provided by the two-step method as the axial view of the reformed space can be seen as an approximation of the orthogonal plane in which the clinical measurements are taken.

7. Automatic Detection of Clinical Landmarks

The segmentation of the dissected aorta, as previously discussed, produces relevant information regarding the FL growth and its extension to branch arteries. The dissection of a branching artery represents a complication of the AD, which requires higher medical attention [62, 63]. The angle between the aorta and a branch artery is indeed known to be a relevant feature for the prediction of late adverse events in AD cases [64, 65]. Hence, in this step, we aim to detect particular aortic landmarks (Figure 1) [26], most of which are located in the proximity of a branch artery. These landmarks have a dual importance:

1. During the follow-up of AD patients, the radiologists measure the diameter of the aorta along normal planes, centered at the landmark position [26]. Nonetheless, every diameter is manually measured; a task which can require up to one hour per patient if performed by an expert;
2. The position of each landmark identifies the nearest branching artery.

Anatomical landmark localisation is an important task in medical image analysis. Accurate landmarks can be used to perform segmentation, feature-based image registration or to detect anatomical structures. A challenging problem is that manual landmarking is very time consuming and the local positioning of the landmarks is highly variable due to the subjective image understanding of different observers. An approach to a more uniform and automatic solution was made by introducing machine learning methods in form of Deep Convolutional Neural Networks (CNN), which should automatically detect anatomical landmarks in medical images. Nonetheless, different kinds of challenging limitations are introduced by this approach. First of all, there is only a limited amount of medical images available due to ethical and financial concerns. Thus, training a CNN becomes a hard task, since overfitting can occur in some cases. This means the network fits the training data too much, decreasing its performance with other non-training data. Secondly, the process of accurate landmarking is, as mentioned before, very time consuming and has to be done by trained specialists to create proper ground truth data for comparison, which is often costly as well.

7.1. State of the art

The detection of anatomical landmarks in medical images has long been a challenging topic; particularly as a preliminary step for image registration and surgery planning [66]. To the best of our knowledge, the detection of aortic landmarks in cases of aortic dissection represents an uncovered clinical and research problem; we therefore provide a general overview of the state of the art for landmark detection in medical imaging. Rueda et al. [67] proposed a landmark detection algorithm based on active appearance models combined with mathematical morphology to detect cephalometric landmarks. Zheng et al. [68] introduced a two-step training based on marginal space learning to

detect anatomical landmarks of the aortic valve. Although the authors claim that this approach could be scaled to other imaging modalities, it has only been tested on cropped thorax images. In 2015, Zheng et al. [69] suggested a further approach for the detection of anatomical landmarks in volumetric data using deep learning. The authors show how the deep learning based method can improve the state of the art by reducing the detection error from 5.97 mm to 2.64 mm on vascular landmarks of the carotid artery in head-and-neck CT scans. The authors use again a two-step approach where a first shallow network is used for testing the volume voxels and extract the most prominent candidates. Afterwards in the second step small 3D patches are extracted from a multi-resolution pyramid. In this step, learned features are used in combination with hand-crafted features obtained used probabilistic boosting-tree. These approaches allow to learn to detect anatomical landmarks without providing prior information of the anatomy. Nonetheless, a limitation of this approach is the requirement of a large collection of training samples necessary to training the high number of network parameters. Li et al. [70] proposed to train a multitask 2D deep neural network on 2.5D representations; the input to the network is a 3-channel 2D patch image where each channel depicts one of the three standard views, axial, sagittal, and coronal. For a generic patch centered in a specific point $P(x,y,z)$, the network is trained to both classify the direction of the displacement vector \mathbf{D} to a specific landmark and predict the magnitude of the vector \mathbf{D} . The method has been designed to reduce the computational requirements of 3D deep neural networks, although this simplification comes at the cost of precision.

Further works have addressed the difficulty to efficiently and robustly train a 3D deep neural network for landmark detection, mainly focusing on techniques based on image-to-image transformation or reinforcement learning. Payer et al. [71] focused on the problem of obtaining a good generalization performance when training a neural network with a contained amount of training samples. They observed how networks which perform image-to-image transformations work generally well also when trained with smaller amounts of training images, i.e. from dozens to a few hundreds. They therefore set this as a heatmap generation problem. A 3D deep neural network learns to generate a 3D heatmap for each of the landmarks of interest; the centroid of the heatmap will be used as landmark position. To overcome hardware restrictions as well as architectural limitations, the authors train the network on slabs of 64 slices. Other works have focused on leveraging the training using reinforcement learning methods. Zhang et al. [72] propose to use a patch-based two-step approach, which first learns to filter candidate patches.

A second branch of research has focused on the role of reinforcement learning for anatomical landmark detection. Ghesu et al. [73] have proposed to train an artificial agent to explore a CT volume using an optimal search path, to solve the problem similarly as Li et al. [70] with the multitask neural network. Vlontzos et al. [74] have extended this approach by considering multiple agents represented by deep Q-networks. An accurate analysis on the role of reinforcement learning with multi-scale and multi-agent settings is provided by Alansary et al. [75].

Although, as listed, different studies have considered the problem of anatomical landmarks, none of these studies has shown a specific focus on aortic landmarks. A more specific focus has been given to cardiac landmarks and aortic valve landmarks [68, 74]. In this work, we focus on these specific eleven landmarks and how state-of-the-art methods perform on such landmarks.

7.2. Adopted method

In this work, we focus on the detection of the landmarks, which describe the descending aorta. Figure 1 shows all the eleven landmarks of interest for the management of aortic pathologies. We evaluate the described methods on the detection of:

1. Sinotubular Junction,
2. Sinuses of Vasalva,
3. Aortic annulus,
4. Middle ascending aorta,
5. Proximal descending aorta,
6. Distal descending aorta,
7. Aorta at proximal aortic arch,
8. Aorta at distal aortic arch,
9. Aorta at celiac axis,
10. Aorta at inferior renal artery,
11. Aorta just above iliac bifurcation.

During a careful examination of our data collection, we observed that only twelve CT scans contained all the eleven annotations. Necessary condition for all the described methods as they rely on fully supervised training. We therefore train our method using all the twelve scans and a leave-one-out cross validation approach. In particular, we evaluate the performance of two possible approaches. First, we evaluate the 2.5D PIN approach from Li et al. [70]; afterwards, we compare this approach with the 3D heat-map regression method from Payer et al. [71]. The results are shown in Table 2. It can be noted how, given the low dissimilarity between the sections of the aorta, the 3D approach shows a lower uncertainty of the results; probably due to the presence of more input information. The higher average error on the 3D approach might be due to the necessary downsampling of the image, a limitation which would be solved with state-of-the-art hardware.

Table 2: Evaluations of the different approaches for landmark detection.

Image Type	Error below 30 mm [%]	Average error [mm]
2.5D Patches	96.6	16.8 ± 5.99
3D Volumes	98.0	19.0 ± 2.54

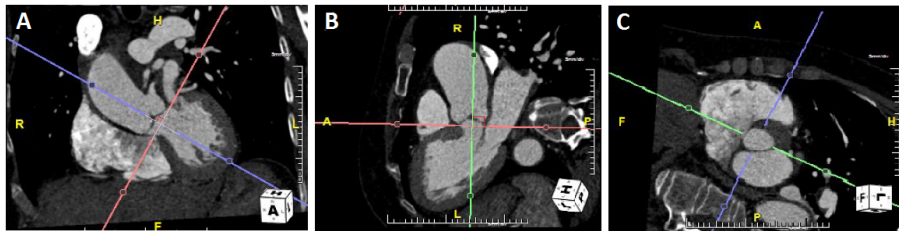


Figure 6: Example of a double-oblique reformation applied to the aortic annulus. The colored planes in A) and B) are adjusted so that they are orthogonal to the aortic annulus from two different orientations. This ensures that the cross-sectional plane in C) is truly orthogonal to the aortic centerline at the specific location [26]

8. Standardized Measurement of Aortic Diameters

In clinical practice, cross-sectional planes are usually defined manually by trained operators using interactive double-oblique reformations (Figure 6) [76], thus, resulting in a user-dependent and time-consuming workflow. A review from Nienaber et al. [77] shows that the inter-observer and intra-observer measurement variabilities for aortic aneurysms are 5 mm and 3 mm, respectively. Variability may be even higher when considering that surgery is recommended at a threshold of 55 mm in case of aortic enlargements [78]. In this scenario, a reproducible workflow may improve aortic surveillance by reducing the measurement uncertainty. In particular, we refer to the possibility of maintaining a constant bias during follow-up examinations, which may be acquired in different clinics.

We here suggest a deep learning approach for the estimation of the cross-sectional plane for user-defined locations without the need for vessel segmentation or tracking. We train and test our approach on 127 and 34 CTA volumes, respectively. Each CTA volume shows imaging data of patients with aortic dissections or aneurysms. For each volume, a trained operator measured the maximum diameters along major and minor axis in the cross-section plane at specific anatomical positions of the aorta, for a total of 3,273 distinct measurements. Each cross-sectional plane was manually defined by an experienced user with the aid of the double-oblique reformation tool offered by Aquarius iNtution (TeraRecon, Inc). In particular, each volume was processed by one out of eleven trained operators. Furthermore, to provide a quantification of inter-

observer variability, twelve of the test volumes were processed three additional times by a subgroup of three different operators. For each measurement location i , we extracted the measurement plane Π_i previously selected by the operator using the double-oblique reformation. Each plane Π_i is individually defined by a point $P_i \in \mathbb{R}^3$ and its unit normal vector \vec{n}_i . Point P_i was chosen by the operator as the pivot of the measurement plane. The estimation of the unit normal vector \vec{n}_i would generally require a regression of the three variables (x, y, z) . To reduce the uncertainty, we use spherical coordinates (r, θ, ϕ) . This representation simplifies the problem to the estimation of the two variables (θ, ϕ) , given we deal with unit vectors. For training and testing, we resampled the CTA volumes to a fixed image spacing of $S = (1.4, 1.4, 1.5)$ mm and normalized the voxel intensity values, θ , and ϕ to a range $I = [0, 1]$.

Data analysis. We analyzed the inter-observer variability of three operators on a subset of 12 CTA volumes. The overall variability of the manual annotations is 4 mm and in line with the literature [77], while the maximum variability between users is 9 mm. To quantify the influence of the plane orientation on these measures, we compared the deviation of the diameters to that of the normal vector (θ, ϕ) of the cross-sectional planes. An overall variability of 4 mm in cross-sectional diameter can be associated with an overall angular variability of the cross-sectional plane of 10.4° for θ and 24.2° for ϕ . For the case of maximum measurement variability of 9 mm, we report a corresponding angular variability of 33.0° for θ and 79.3° for ϕ .

Neural network. We define a CNN architecture (Figure 7), which learns the distribution of the annotations performed by the operators. The network is trained to predict the orientation of the cross-sectional plane (θ, ϕ) , given a surrounding patch \vec{V} of size $64 \times 64 \times 64$. The motivation for such size is given by the intrinsic shape of the aorta, which can extend in different directions when ranging from its initial ascending trait and down to the abdomen. To provide an estimation of the network uncertainty we use a Bayesian approximation provided by the dropout layers[79].

Results. We trained our model on 127 CTA images and a total of 2,556 measurements. Each measurement patch has been augmented during training with rotation or translation. We used a batch size of $b = 64$ and a learning rate of $l_r = 0.003$. The training was terminated after 16 epochs using an early-stopping approach. The results are reported in Table 3. In particular, it can be noticed how a CNN can be able to retrieve the cross-sectional view with human accuracy as the average error is within the human error range and substantially lower than that from the human operator with the highest disagreement.

9. Shape completion for disease regression

In this section, we address the shortage of CTA images in the pre-pathological stage. We address this shortage using image processing via generative adver-

Table 3: Neural network results on test set. The execution strategy is evaluated over a different number of iterations k .

k	Huber loss	θ -error [deg]	ϕ -error [deg]
1	0.044	11.95	32.08
5	0.043 ± 0.01	6.78 ± 6.15	18.77 ± 15.71
10	0.039 ± 0.01	5.93 ± 4.30	13.38 ± 10.45
20	0.040 ± 0.01	5.31 ± 2.77	19.69 ± 7.63

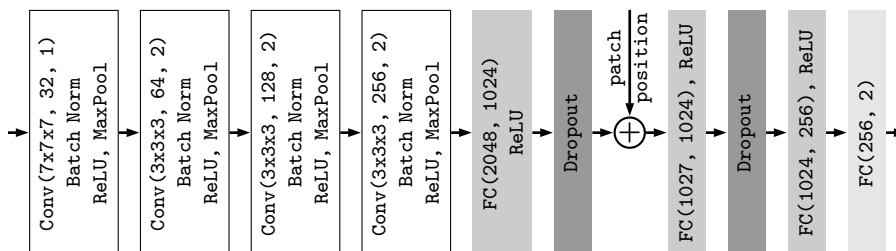


Figure 7: Illustration of the used for the regression task. Legend: Conv(K, D, S) – convolution with kernel K, stride S, and D output channels; FC(X, Y) – fully connected layer with X inputs and Y outputs; Patch position – relative position of the patch in the CTA volume.

serial networks (GANs) [80], which have already found applications in different research areas, such as image completion [81] and image artifact reduction [82]. To date, most of those applications deal with 2D RGB images or, in medical scenario, 2D axial images. By using a free-form 3D inpainting approach we are here able to generate plausible pre-dissection CTA datasets. We consider the FL of an AD as an image ‘artifact’ to be masked for removal.

9.1. Pre-processing

To minimize the computational cost of this operation, the datasets were cropped to a variable size of approximate $100 \times 100 \times D$ voxels, with the number of slices, D , depending on the length of the aorta. The extent of the smallest cropped volume is $100 \times 100 \times 133$, whereas the extent of the largest is $104 \times 104 \times 473$. As a result, all images contain only the descending aorta and its immediate surroundings. This decision has been taken as we primarily focus on Type-B AD. An extension to Type-A would be possible by applying the curved planar reformation techniques during the pre-processing phase.

9.2. Method

Aortic dissection (AD) can extend along the whole aorta. For this reason, inpainting techniques can easily fail when considering single 2D slices. Therefore, we define a novel 3D inpainting method based on a two-stage GAN. Each

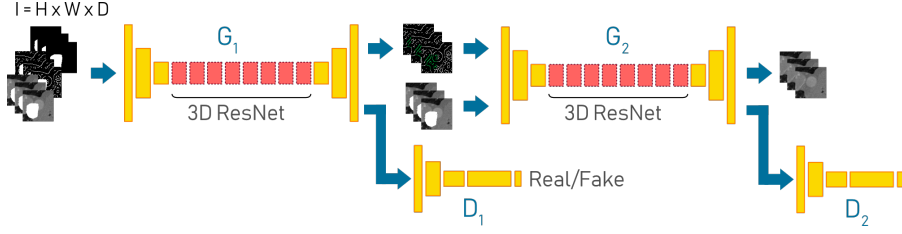


Figure 8: Architecture of the two-stage 3D network. Each input volume has size I . In yellow, the convolution and deconvolution layers. In red, the residual blocks.

stage consists of a 3D-GAN with spectral normalization [83]. In both stages, the discriminators and the generators follow the general architecture suggested by Nazeri et al. [81], where we replace the 2D convolutions and instance normalizations with 3D operators. Also the residual blocks are replaced with 3D residual blocks (Figure 8). The network input is obtained from a 3D patch, \mathbf{V} , of size $I = 100 \times 100 \times 12$; this can be interpreted as a 3D sliding window, \mathbf{V} , which slides along the descending aorta.

Given the 3D patch \mathbf{V} , its edges $\mathbf{C} = \text{edge}(\mathbf{V})$ and a mask \mathbf{M} ; we define the following inputs and output for the first generator G_1 :

$$\mathbf{C}_M = \mathbf{C} \odot (1 - \mathbf{M}), \quad (1)$$

$$\mathbf{V}_M = \mathbf{V} \odot (1 - \mathbf{M}), \quad (2)$$

$$\mathbf{C}_G = G_1(\mathbf{V}_M, \mathbf{C}_M, \mathbf{M}), \quad (3)$$

where \odot is the element-wise product; \mathbf{C}_M , the masked edge volume; \mathbf{V}_M , the masked original volume, and \mathbf{C}_G , the output of the first generator, which contains the reconstructed edges. The output volume \mathbf{C}_G is then used to evaluate the adversarial loss, \mathcal{L}_{adv1} , and the feature matching loss, \mathcal{L}_{FM} , used in the objective function. In particular, having defined with \mathbb{E} the expectation operator,

$$\mathcal{L}_{adv1} = \mathbb{E}_{(\mathbf{C}, \mathbf{V})} [\log D_1(\mathbf{C}, \mathbf{V})] + \mathbb{E}_{(\mathbf{V})} \log [1 - D_1(\mathbf{C}_G, \mathbf{V})] \quad (4)$$

defines a metric of the average distance between the two distributions $(\mathbf{C}_G, \mathbf{V})$ and (\mathbf{C}, \mathbf{V}) .

$$\mathcal{L}_{FM} = \mathbb{E} \left[\sum_{i=1}^L \frac{1}{N_i} \left\| D_1^{(i)}(\mathbf{C}) - D_1^{(i)}(\mathbf{C}_G) \right\|_1 \right] \quad (5)$$

defines a metric in the feature space; where L is the number of convolution layers in the discriminators, $D_1^{(i)}$ is the activation of layer i . Similar volumes should therefore have similar activation maps. This information is then combined in the adversarial objective function:

$$\min_{G_1} \max_{D_1} \mathcal{L}_{G_1} = \min_{G_1} \left[\lambda_{adv1} \max_{D_1} (\mathcal{L}_{adv1}) + \lambda_{FM} \mathcal{L}_{FM} \right], \quad (6)$$

where λ_{adv1} and λ_{FM} are regularization parameters. We extend this evaluation also to the second generator, G_2 :

$$\mathbf{C}_I = \mathbf{C}_M + \mathbf{C}_G \odot \mathbf{M}, \quad (7)$$

$$\mathbf{V}_G = G_2(\mathbf{V}_M, \mathbf{C}_I), \quad (8)$$

$$\mathbf{V}_I = \mathbf{V}_M + \mathbf{V}_G \odot \mathbf{M}, \quad (9)$$

where \mathbf{C}_I represents the inpainting of \mathbf{C}_M ; \mathbf{V}_G , the output of the second generator, and \mathbf{V}_I , the final inpainting of \mathbf{V}_M .

Ad-hoc loss functions have been defined for 2D image outputs. These include the style loss and the perceptual loss [84], which provide a metric based on the activation maps of a pre-trained VGG-19 network. Practical experiments revealed that the distances in the feature space are not significantly affected by the dataset used to train the network. Nonetheless, the VGG-19 network is trained on 2D RGB images; therefore we introduced an averaged perceptual loss and style loss,

$$\mathcal{L}_{perc,av} = \mathbb{E} \left[\sum_{i,j} \frac{1}{N_i} \|\phi_i(\mathbf{I}_j) - \phi_i(\mathbf{I}_{G_j})\|_1 \right], \quad (10)$$

$$\mathcal{L}_{style,av} = \mathbb{E}_{k,j} \left[\|G_k^\phi(\mathbf{I}_j) - G_k^\phi(\mathbf{I}_{G_j})\|_1 \right], \quad (11)$$

where we compute the loss values on a per-slice level j and average them over the input and output volumes. This considers the fact that medical experts generally evaluate the volume by analyzing single 2D axial views. Each ϕ_i is the activation map of the layer i in the VGG-19 network; G_k^ϕ is a Gram matrix derived from the activation map ϕ_k [84]. Thus, we define a composite objective function:

$$\min_{G_2} \max_{D_2} \mathcal{L}_{G_2} = \min_{G_2} \max_{D_2} [\lambda_{adv2} \mathcal{L}_{adv2} + \lambda_{l_1} \mathcal{L}_{l_1} + \lambda_p \mathcal{L}_{perc,av} + \lambda_s \mathcal{L}_{style,av}] \quad (12)$$

where λ_{adv2} , λ_{l_1} , λ_p , and λ_s are regularization parameters; \mathcal{L}_{adv2} is the adversarial loss (Eq. 4), and \mathcal{L}_{l_1} is the L1 loss. Previously, examples of 2D inpainting networks were trained with the masks provided by Liu et al. [85] or more simply with rectangular masks [85, 81]. In this work, we generate random 3D masks by filling each of the 12 slices randomly with a mask from the dataset provided by Liu et al., a random super-ellipse (SE), or a segmentation mask. During training, the masks and the patch volumes are selected randomly. During testing, the patch volumes are consecutively extracted with a sliding window, together with the relative masks, with a pace of four slices.

9.3. Experiments and results

To evaluate our approach, we train the network on cropped regions of interest (ROI) from 55 non-dissected aortae, which we augment through reflections, as the descending aorta can be situated on both sides of the spine. We evaluate

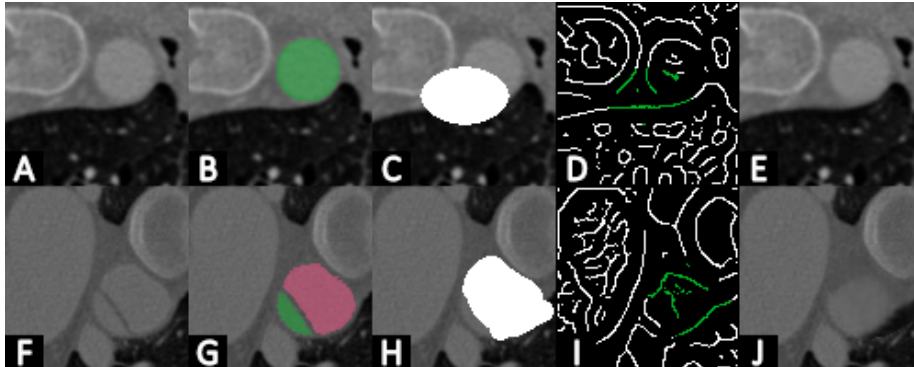


Figure 9: Example of two inpainted slices. A) A healthy aorta, F) A dissected aorta, B) G) Segmentation of true lumen (green) and false lumen (red), C) H) masked image, D) I) hallucinated edges (green), E) J) inpainting result on the aorta and surroundings.

Table 4: Quantitative results of the inpainting, compared to the previous 2D version [81]. Precision (Prec.) and Accuracy (Acc.) refer to the edge reconstruction.

Input	Mask	Prec.	Acc.	\mathcal{L}_{l_1}	$\mathcal{L}_{perc,av}$	$\mathcal{L}_{style,av}$	HDD	PSNR	MAE
2D	SE	32.26	28.64	0.349	0.048	0.065	0.610	30.465	0.017
2D	SE/FF	10.32	10.34	0.192	0.099	0.102	1.248	17.049	0.186
3D	SE	58.89	55.44	0.261	0.045	0.020	0.082	45.898	0.003
3D	SE/FF	88.67	86.53	0.201	0.049	0.027	0.168	41.81	0.005

its performance over a separate pool of 20 images of non-dissected aortae, to be able to quantify the results. Moreover, we test our approach with after-AD images and ask medical experts to evaluate the results.

The training was performed using PyTorch (version 1.3.0) on a desktop computer (equipped with a CPU Intel i7-8700, 64GB RAM, and a GPU NVIDIA Titan RTX with 24GB VRAM) and with a batch size of 16. The learning rate was set to 10^{-4} , λ_{adv1} and λ_{adv2} to 0.1, λ_{FM} to 10, λ_s to 250, λ_{l_1} to 1 and λ_p to 0.1. The networks have been trained for approximately 24 hours.

Initially, we only train the first stage, where the volume edges are reconstructed. First, we train with stacks of random SE to provide the training with more degrees of freedom than the usual rectangles. We continue training by mixing the SE slices with the free-form masks from Liu et al. [85] and further segmentation masks of medical images. We refer to this combination as FF.

Table 4 summarizes the measured precision and accuracy for this stage. The 3D information enhances the performances considerably, especially, for FF. Probably due to the high size and shape variety of masks, the 3D approach outperformed the 2D approach. Convolution in 3D can use information from adjacent slices, resulting in a network capable of inpainting in larger planar areas.

We repeat the same experiments for the second stage. Here, precision and recall may not be reliable measures, as small differences are acceptable. Therefore, we evaluate the performance of the inpainting stage using the loss metrics, together with the peak signal-to-noise ratio (PSNR), the mean absolute error (MAE) and the Hausdorff distance (HDD).

The measures in Table 4 show a trend comparable with the first stage. In both the experiments, the 3D approach provided results, which are visibly more accurate. Nonetheless, a detailed comparison between the two trends shows that there is still space for improvements in the second stage. Figure 9 provides a visual overview of the results. The images of the resulting pre-dissection case were reviewed by a cardiovascular radiologist with more than 20 years of experience in the interpretation of CT angiograms of patients with aortic diseases. The expert was asked to evaluate if the virtual pre-dissection aorta reasonably resembled the expected appearance of non-diseased aorta. Specifically, the expert was asked to assess if the following key features of a dissection were suppressed in the virtual pre-dissection dataset: (a) Presence of a dissection flap, (b) difference in contrast enhancement between TL and FL, (c) shape of the outer contour of the aorta, and (d) introduced artifacts or unexpected findings.

- (a) The dissection flap—the diagnostic hallmark of aortic dissection in CT—was successfully eliminated in almost all images.
- (b) The contrast opacification of the simulated pre-dissection aorta appeared homogeneous, with elimination of the typical attenuation difference between TL versus FL blood. There is a contrast heterogeneity without an abrupt transition caused by a dissection flap. The contrast heterogeneity exhibits commonly observed mixing artifacts.
- (c) The shape of the virtual pre-dissection aorta was considered remarkably similar to the expected appearance of a normal aorta, with circular or slightly oval cross section on transverse CT images, with coronal and sagittal reformats. This is in contradiction to the typically more eccentric shape of a dissected aorta, where the outer wall of the FL stretches and dilates due to thinning and loss of elastic tissue.

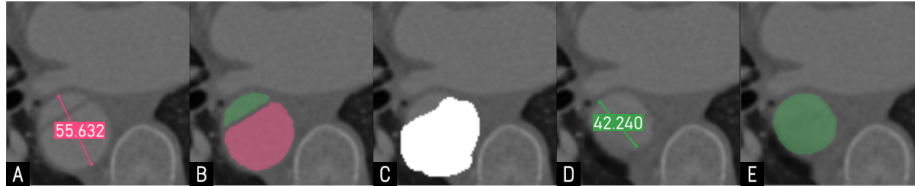


Figure 10: Example of size change during AD regression. Values in millimeter. A) Original image. The aorta presents a higher diameter due to the presence of the FL, B) Segmentation of TL (green) and FL (red), C) Masked image, D) Reconstructed pre-dissection state. The diameter is now lower. E) Segmentation of the pre-dissection aorta.

- (d) Even though, subjectively, the appearance of the virtual regression was remarkably similar to a non-dissected aorta, the interface between the inserted aorta and its surrounding (typically a few millimeter outside of the aortic contour) was noticeable (see Figure 10). However, these artifacts did not distract from the evaluation of the important features of the aorta.

10. Conclusion

In this work, we have examined innovative methods to segment the true and false lumina of dissected aortae in CTA volumes; in particular, we discussed two possible deep learning-based approaches, depending on the designated usage. To support the clinical work on aortic surveillance and to register the follow-up examinations we have defined an approach for the detection of pre-defined landmarks, which allow both to measure the aortic diameter at specific locations, by using the vessel's centerline obtained using the overall AD segmentation, and to register such volumes to quantify the physical changes. Finally, we proposed an approach to estimate the original shape and size of a dissected aorta based on the learnt statistical shape of healthy aortae. An expert clinician has been asked to analyze the reconstructed images. Furthermore, some of the algorithms here discussed have been made available online on the public web platform Studierfenster (<http://studierfenster.tugraz.at/>) [86]. Future work will see the possibility of predicting the growth of the disease and the relative speed, as well as techniques to more accurately and robustly measure the overall diameter. These simulated models can be used to support biomechanical research, which deals with understanding the causes of the pathology. Furthermore, to leverage the clinical efforts, further work may see the application of weak training strategies to overcome the problem of incomplete training data for landmark detection.

Acknowledgement

This work would not have been possible without the TU Graz LEAD Project (Mechanics, Modeling and Simulation of Aortic Dissection) and the connection established by Prof. Dr. Gerhard Holzapfel from Graz University of Technology. An acknowledgment goes also to Dr. Gabriel Mistelbauer from the University of Magdeburg, Dr. Domenico Mastrodicasa, Dr. Martin Willeminck, Mr. Shannon Walters, Virginia Hinojosa, Valery Turner and Chris Le Castillo from Stanford University for the support provided during the research stay at Stanford Medicine. Furthermore, an acknowledgment goes to the Austrian Marshall Plan Foundation for the Marshall Plan Scholarship n. 942121022222019.

References

- [1] C. Lau, D. N. Feldman, L. N. Girardi, L. K. Kim, Epidemiology of thoracic aortic dissection, *Journal of Thoracic Disease* 9 (4) (2017) S309–S316. doi : 10.21037/jtd.2017.03.89.

- [2] P. Rajiah, Ct and mri in the evaluation of thoracic aortic diseases, *International Journal of Vascular Medicine* 2013 (797189) (2013) 1–16. doi:
<https://doi.org/10.1155/2013/797189>.
- [3] N. Kontopodis, S. Lioudaki, D. Pantidis, G. Papadopoulos, E. Georgakarakos, C. V. Ioannou, Advances in determining abdominal aortic aneurysm size and growth, *World Journal of Radiology* 8 (2) (2016) 148–158. doi:10.4329/wjr.v8.i2.148.
- [4] Z. S. Gamechi, L. R. Bons, M. Giordano, D. Bos, R. P. J. Budde, K. F. Kofoed, J. H. Pedersen, J. W. Roos-Hesselink, M. de Bruijne, Automated 3d segmentation and diameter measurement of the thoracic aorta on non-contrast enhanced ct, *European Radiology* 29 (9) (2019) 4613–4623. doi:
10.1007/s00330-018-5931-z.
- [5] K. Krissian, J. M. Carreira, J. Esclarin, M. Maynar, Semi-automatic segmentation and detection of aorta dissection wall in mdct angiography, *Medical Image Analysis* 18 (1) (2014) 83–102. doi:<https://doi.org/10.1016/j.media.2013.09.004>.
- [6] J. Egger, S. Gunacker, A. Pepe, et al., A comprehensive workflow and framework for immersive virtual endoscopy of dissected aortae from cta data, in: *SPIE Medical Imaging* 1131531, 2020. doi:10.1117/12.2559239.
- [7] S. Sherifova, G. Sommer, C. Viertler, P. Regitnig, T. Caranasos, M. A. Smith, B. E. Griffith, R. W. Odgen, G. A. Holzapfel, Failure properties and microstructure of healthy and aneurysmatic human thoracic aortas subjected to uniaxial extension with a focus on the media, *Acta Biomaterialia* doi:10.1016/j.actbio.2019.08.038.
- [8] D. P. Howard, A. Banerjee, J. F. Fairhead, et al., Population-based study of incidence and outcome of acute aortic dissection and premorbid risk factor control: 10-year results from the oxford vascular study, *Circulation* 127 (20) (2013) 2031–2037. doi:10.1161/circulationaha.112.000483.
- [9] S. A. LeMaire, L. Russell, Epidemiology of thoracic aortic dissection, *Nature Reviews Cardiology* 8 (2) (2011) 103–113. doi:10.1038/nrcardio.2010.187.
- [10] S. Sherifova, G. A. Holzapfel, Biomechanics of aortic wall failure with a focus on dissection and aneurysm: A review, *Acta Biomaterialia* doi:10.1016/j.actbio.2019.08.017.
- [11] E. Krol, J. M. Panneton, Uncomplicated acute type b aortic dissection: Selection guidelines for tevar, *Annals of Vascular Diseases* 10 (3) (2017) 165–169.
- [12] A. Pepe, J. Li, M. Rolf-Pissarczyk, et al., Detection, segmentation, simulation and visualization of aortic dissections: A review, *Medical Image Analysis* doi:10.1016/j.media.2020.101773.

- [13] J. Egger, Z. Mostarkic, S. Großkopf, B. Freisleben, Preoperative measurement of aneurysms and stenosis and stentsimulation for endovascular treatment, 2007 4th IEEE International Symposium on Biomedical Imaging: From Nano to Macro (2007) 392–395.
- [14] J. Egger, S. Großkopf, C. Nimsy, T. Kapur, B. Freisleben, Modeling and visualization techniques for virtual stenting of aneurysms and stenoses, *Computerized medical imaging and graphics : the official journal of the Computerized Medical Imaging Society* 36 3 (2012) 183–203.
- [15] M. D. Dake, N. Kato, R. S. Mitchell, C. P. Semba, M. K. Razavi, T. Shimonono, T. Hirano, K. Takeda, I. Yada, D. C. Miller, Endovascular stent-graft placement for the treatment of acute aortic dissection., *New England Journal of Medicine* 340 (20) (1999) 1546.
- [16] C. Y. Huang, S. H. Weng, C. F. Weng, W. Y. Chen, I. M. Chen, C. P. Hsu, C. C. Shih, Factors predictive of distal stent graft-induced new entry after hybrid arch elephant trunk repair with stainless steel-based device in aortic dissection, *Journal of Trauma-injury Infection and Critical Care* 146 (3) (2013) 623–630.
- [17] F. Rohlfes, N. Tsilimparis, H. Diener, A. Larena-Avellaneda, V. Kodolitsch, Y. S. Wipper, E. S. Debus, T. Kölbel, Chronic type b aortic dissection: indications and strategies for treatment, *Journal of Cardiovascular Surgery* 56 (2) (2015) 231.
- [18] C. A. Nienaber, S. Kische, H. Rousseau, H. Eggebrecht, T. C. Rehders, G. Kundt, A. Glass, D. Scheinert, M. Czerny, T. Kleinfeldt, Endovascular repair of type b aortic dissection: long-term results of the randomized investigation of stent grafts in aortic dissection trial, *Clinical Misdiagnosis and Mistherapy* 6 (3) (2014) 407.
- [19] Q. Lu, J. Feng, J. Zhou, Z. Zhao, H. Li, Z. Teng, Z. Jing, Endovascular repair by customized branched stent-graft: A promising treatment for chronic aortic dissection involving the arch branches, *Journal of Thoracic and Cardiovascular Surgery* 150 (6) (2015) 1631–1638.e5.
- [20] J. Lu, J. Egger, A. Wimmer, S. Großkopf, B. Freisleben, Detection and visualization of endoleaks in ct data for monitoring of thoracic and abdominal aortic aneurysm stents, in: *Medical Imaging: Image-Guided Procedures*, 2008.
- [21] S. S. Parmer, J. P. Carpenter, S. W. Stavropoulos, R. M. Fairman, A. Pochettino, E. Y. Woo, G. W. Moser, J. E. Bavaria, Endoleaks after endovascular repair of thoracic aortic aneurysms, *Journal of Vascular Surgery* 44 (3) (2006) 447–452.
- [22] S. Huptas, R. H. Mehta, H. Köhl, K. Tsagakis, N. Reinsch, P. Kahlert, H. G. Jakob, R. Erbel, H. Eggebrecht, Aortic remodeling in type b aortic

- dissection: effects of endovascular stent-graft repair and medical treatment on true and false lumen volumes, *Journal of Endovascular Therapy* 140 (3) (2009) 28–38.
- [23] K. M. Kim, C. E. Donayre, T. S. Reynolds, G. E. Kopchok, I. Walot, J. P. Chauvapun, R. A. White, Aortic remodeling, volumetric analysis, and clinical outcomes of endoluminal exclusion of acute complicated type b thoracic aortic dissections, *Journal of Vascular Surgery* 54 (2) (2011) 316–325.
- [24] G. Melissano, L. Bertoglio, E. Rinaldi, E. Civilini, Y. Tshomba, A. Kahlberg, E. Agricola, R. Chiesa, Volume changes in aortic true and false lumen after the "petticoat" procedure for type b aortic dissection, *Journal of Vascular Surgery* 55 (3) (2012) 641–651.
- [25] S. Maria, C. Martin, C. Manfred, R. Thomas, S. Alfred, G. H. Sodeck, G. Roman, L. Christian, L. Johannes, Endovascular repair of acute type b aortic dissection: long-term follow-up of true and false lumen diameter changes, *Annals of Thoracic Surgery* 83 (3) (2007) 1059–1066.
- [26] V. Hinostroza, S. Walters, K. Raman, M. Fischbein, L. Molvin, D. Fleischmann, Aortic Surveillance Program: An Interdisciplinary and Standardized Approach to Comprehensive Imaging and Monitoring of Aortic Dissections, 2018.
- [27] Y. LeCun, Y. Bengio, G. Hinton, Deep learning, *Nature* 521 (2015) 436–444. doi:10.1038/nature14539.
- [28] M. Weber, D. Wild, J. Wallner, J. Egger, A client/server based online environment for the calculation of medical segmentation scores, 2019. doi:10.1109/EMBC.2019.8856481.
- [29] J. Li, A. Pepe, C. Gsaxner, J. Egger, An online platform for automatic skull defect restoration and cranial implant design, *CoRR abs/2006.00980*. URL <http://arxiv.org/abs/2006.00980>
- [30] K. Higashigaito, A. M. Sailer, S. M. J. van Kuijk, M. J. Willemink, L. D. Hahn, T. J. Hastie, D. Craig Miller, M. P. Fischbein, D. Fleischmann, Aortic growth and development of partial false lumen thrombosis are associated with late adverse events in type b aortic dissection, *The Journal of Thoracic and Cardiovascular Surgery*.
- [31] M. Masoudi, H.-R. Pourreza, M. S.-T. and others, A new dataset of computed-tomography angiography images for computer-aided detection of pulmonary embolism, *Scientific Data* 5 (2018) 180180.
- [32] D. Lesage, E. D. Angelini, I. Bloch, F. L. Gareth, A review of 3d vessel lumen segmentation techniques: Models, features and extraction schemes, *Medical Image Analysis* 13 (6) (2009) 819–845.

- [33] S. Kurugol, R. S. J. Estepar, J. Ross, G. R. Washko, Aorta segmentation with a 3d level set approach and quantification of aortic calcifications in non-contrast chest ct, in: International Conference of the IEEE Engineering in Medicine and Biology Society, 2012, p. 2343.
- [34] J. A. Martínez-Mera, P. G. Tahoces, J. M. Carreira, A hybrid method based on level set and 3d region growing for segmentation of the thoracic aorta., *Computer Aided Surgery* 18 (5-6) (2013) 109–117.
- [35] N. A. Seada, S. Hamad, M. G. M. Mostafa, Automatically seeded region growing approach for automatic segmentation of ascending aorta, in: International Conference on Informatics and Systems, 2016, pp. 127–132.
- [36] N. Seada, S. Hamad, M. G. Mostafa, Model-based automatic segmentation of ascending aorta from multimodality medical data, *International Journal of Electrical and Computer Engineering* 6 (6).
- [37] T. Behrens, K. Rohr, H. S. Stiehl, Robust segmentation of tubular structures in 3-d medical images by parametric object detection and tracking., *IEEE Transactions on Systems Man and Cybernetics Part B Cybernetics A Publication of the IEEE Systems Man and Cybernetics Society* 33 (4) (2003) 554.
- [38] Y. Xie, J. Padgett, A. Biancardi, A. Reeves, Automated aorta segmentation in low-dose chest ct images., *International Journal of Computer Assisted Radiology and Surgery* 9 (2) (2014) 211–219.
- [39] P. J. Lubniewski, B. Miguel, V. Sauvage, C. Lohou, Interactive 3d segmentation by tubular envelope model for the aorta treatment, *Proceedings of SPIE - The International Society for Optical Engineering* 8290 (9) (2012) 841–845.
- [40] D. Vitanovski, K. Ralovich, R. Ionasec, Y. Zheng, M. Suehling, W. Krawtschuk, J. Hornegger, D. Comaniciu, Personalized learning-based segmentation of thoracic aorta and main branches for diagnosis and treatment planning, in: *IEEE International Symposium on Biomedical Imaging*, 2012, pp. 836–839.
- [41] J. Noothout, B. D. Vos, J. Wolterink, I. Isgum, Automatic segmentation of thoracic aorta segments in low-dose chest ct, in: *Image Processing*, 2018, p. 63.
- [42] R. Trullo, C. Petitjean, S. Ruan, B. Dubray, D. Nie, D. Shen, Segmentation of organs at risk in thoracic ct images using a sharpmask architecture and conditional random fields, *Proc IEEE Int Symp Biomed Imaging*. (2017) 1003–1006.
- [43] C. A. Morariu, D. S. Dohle, T. Terheiden, K. Tsagakakis, J. Pauli, Polar-based aortic segmentation in 3d cta dissection data using a piecewise constant curvature model, in: *Bildverarbeitung für die Medizin*, 2014.

- [44] T. Kovács, P. Cattin, H. Alkadhi, S. Wildermuth, G. Székely, Automatic Segmentation of the Vessel Lumen from 3D CTA Images of Aortic Dissection, Springer Berlin Heidelberg, 2006.
- [45] T. Kovács, P. Cattin, H. Alkadhi, S. Wildermuth, G. Székely, Automatic segmentation of the aortic dissection membrane from 3d cta images, in: International Conference on Medical Imaging and Augmented Reality, 2006, pp. 317–324.
- [46] M. Descoteaux, M. Audette, K. Chinzei, K. Siddiqi, Bone enhancement filtering: Application to sinus bone segmentation and simulation of pituitary surgery, in: J. S. Duncan, G. Gerig (Eds.), Medical Image Computing and Computer-Assisted Intervention – MICCAI 2005, Springer Berlin Heidelberg, Berlin, Heidelberg, 2005, pp. 9–16.
- [47] Kovács, Automatic segmentation of the vessel lumen from 3D CTA images of aortic dissection, Vol. 065, Hartung-Gorre Verlag, 2010. doi:<https://doi.org/10.3929/ethz-a-006214181>.
- [48] N. Fetnaci, P. Lubniewski, B. Miguel, C. Lohou, 3d segmentation of the true and false lumens on ct aortic dissection images, Proceedings of SPIE - The International Society for Optical Engineering 8650 (4) (2013) –.
- [49] N. Lee, H. Tek, A. F. Laine, True-false lumen segmentation of aortic dissection using multi-scale wavelet analysis and generative-discriminative model matching, Proceedings of SPIE - The International Society for Optical Engineering 6915 (2008) 69152V–69152V–11.
- [50] H. Tek, A. Ayvaci, D. Comaniciu, Multi-scale vessel boundary detection, in: CVBIA, 2005.
- [51] O. Ronneberger, P. Fischer, T. Brox, U-net: Convolutional networks for biomedical image segmentation 9351 (2015) 234–241.
- [52] F. Milletari, N. Navab, S. A. Ahmadi, V-net: Fully convolutional neural networks for volumetric medical image segmentation, in: Fourth International Conference on 3d Vision, 2016, pp. 565–571.
- [53] X. Li, H. Chen, X. Qi, Q. Dou, C. Fu, P. Heng, H-denseunet: Hybrid densely connected unet for liver and tumor segmentation from ct volumes, IEEE Transactions on Medical Imaging 37 (12) (2018) 2663–2674.
- [54] C. Gsaxner, B. Pfarrkirchner, et al., Pet-train: Automatic ground truth generation from pet acquisitions for urinary bladder segmentation in ct images using deep learning, in: Proc. of IEEE Biomedical Engineering International Conference, 2018, pp. 1–5.
- [55] A. Pepe, et al., Iris: interactive real-time feedback image segmentation with deep learning, in: Proc. of SPIE Medical Imaging, 2020.

- [56] Z. Li, J. Feng, Z. Feng, Y. An, Y. Gao, B. Lu, J. Zhou, Lumen segmentation of aortic dissection with cascaded convolutional network, in: M. Pop, M. Sermesant, J. Zhao, S. Li, K. McLeod, A. Young, K. Rhode, T. Mansi (Eds.), *Statistical Atlases and Computational Models of the Heart. Atrial Segmentation and LV Quantification Challenges*, Springer International Publishing, Cham, 2019, pp. 122–130.
- [57] C. Long, S. Ruiqiong, G. Yangyang, X. Lei, Z. Panli, J. Yan, L. Jie, H. Yuan, W. Xinhao, L. Shaoliang, C. Xiangfei, G. Wei, Fully automatic segmentation of type b aortic dissection from cta images enabled by deep learning., *European Journal of Radiology* 121.
- [58] Z. Gu, J. Cheng, H. F. andKang Zhou, H. Hao, Y. Z. andTianyang Zhang, S. Gao, J. Liu, Ce-net: Context encoder network for 2d medical image segmentation, *IEEE Transactions on Medical Imaging* 38 (10) (2019) 2281–2292.
- [59] C. Long, S. Ruiqiong, G. Yangyang, X. Lei, Z. Panli, J. Yan, L. Jie, H. Yuan, W. Xinhao, L. Shaoliang, C. Xiangfei, G. Wei, Distance transformations in digital images, *Computer Vision, Graphics, and Image Processing* 34 (3) (1986) 344–371.
- [60] A. Kanitsar, D. Fleischmann, R. Wegenkittl, P. Felkel, M. E. Groeller, Cpr: curved planar reformation, 2002, pp. 37–44.
- [61] L. Yu, X. Yang, H. Chen, J. Qin, P.-A. Heng, Volumetric convnets with mixed residual connections for automated prostate segmentation from 3d mr images, 2017.
- [62] S. Lentini, F. Tancredi, F. Benedetto, R. Gaeta, Type A aortic dissection involving the carotid arteries: carotid stenting during open aortic arch surgery, *Interactive CardioVascular and Thoracic Surgery* 8 (1) (2009) 157–159.
- [63] Z. Wang, A. C. Bovik, H. R. Sheikh, E. P. Simoncelli, Image quality assessment: from error visibility to structural similarity, *IEEE Transactions on Image Processing* 13 (2004) 600–612.
- [64] A. Shirali, M. Bischoff, et al., Predicting the Risk for Acute Type B Aortic Dissection in Hypertensive Patients Using Anatomic Variables, *JACC Cardiovascular Imaging* 6 (3) (2013) 349–357.
- [65] D. M. Williams, P. Cronin, et al., Aortic Branch Artery Pseudoaneurysms Accompanying Aortic Dissection. Part II. Distinction from Penetrating Atherosclerotic Ulcers, *Journal of Vascular and Interventional Radiology* 17 (5) (2006) 773–781.
- [66] M. Betke, H. Hong, D. Thomas, C. Prince, J. P. Ko, Landmark detection in the chest and registration of lung surfaces with an application to nodule registration, *Medical Image Analysis* 7 (3) (2003) 265–281.

- [67] S. Rueda, M. Alcañiz, An approach for the automatic cephalometric landmark detection using mathematical morphology and active appearance models, in: International Conference on Medical Image Computing and Computer-Assisted Intervention, 2006, pp. 159–166.
- [68] Y. Zheng, M. John, R. Liao, J. Boese, U. Kirchstein, B. Georgescu, S. K. Zhou, J. Kempfert, T. Walther, G. Brockmann, D. Comaniciu, Automatic aorta segmentation and valve landmark detection in c-arm ct: Application to aortic valve implantation, in: International Conference on Medical Image Computing and Computer-Assisted Intervention, 2010, pp. 476–483.
- [69] Y. Zheng, D. Liu, B. Georgescu, H. Nguyen, D. Comaniciu, 3d deep learning for efficient and robust landmark detection in volumetric data, in: International Conference on Medical Image Computing and Computer-Assisted Intervention, 2015, pp. 565–572.
- [70] Y. Li, A. Alansary, J. J. Cerrolaza, B. Khanal, M. Sinclair, J. Matthew, C. Gupta, C. Knight, B. Kainz, D. Rueckert, Fast multiple landmark localisation using a patch-based iterative network, in: International Conference on Medical Image Computing and Computer-Assisted Intervention, 2018, pp. 563–571.
- [71] C. Payer, D. Štern, H. Bischof, M. Urschler, Integrating spatial configuration into heatmap regression based CNNs for landmark localization, *Medical Image Analysis* 54 (2019) 207–219.
- [72] J. Zhang, M. Liu, D. Shen, Detecting Anatomical Landmarks From Limited Medical Imaging Data Using Two-Stage Task-Oriented Deep Neural Networks 26 (10) (2017) 4753–4764.
- [73] F. C. Ghesu, et al., Multi-Scale Deep Reinforcement Learning for Real-Time 3D-Landmark Detection in CT Scans, *IEEE Transactions on Pattern Analysis and Machine Intelligence* 41 (6) (2019) 176–189.
- [74] A. Vlontzos, A. Alansary, K. Kamnitsas, D. Rueckert, B. Kainz, Multiple landmark detection using multi-agent reinforcement learning, in: International Conference on Medical Image Computing and Computer-Assisted Intervention, 2018, pp. 262–270.
- [75] A. Alansary, et al., Evaluating reinforcement learning agents for anatomical landmark detection, *Medical Image Analysis* 53 (2019) 156–164.
- [76] E. Díaz-Peláez, M. Barreiro-Pérez, A. Martín-García, P. L. Sanchez, Measuring the aorta in the era of multimodality imaging: still to be agreed, *Journal of Thoracic Disease* 9 (6) (2017) S445–S447. doi:10.21037/jtd.2017.03.96.
- [77] C. A. Nienaber, R. E. Clough, N. Sakalihasan, T. Suzuki, R. Gibbs, F. Mussa, M. P. Jenkins, M. M. Thompson, A. Evangelista, J. S. Yeh,

- N. Cheshire, U. Rosendahl, J. Pepper, Aortic dissection, *Nature Reviews Disease Primers* 21 (2) (2016) 16053. doi:10.1038/nrdp.2016.53.
- [78] S. Heuts, B. P. Adriaans, B. Rylski, C. Muhl, S. C. A. M. Bekkers, J. R. Olsthoorn, E. Natour, et al., Evaluating the diagnostic accuracy of maximal aortic diameter, length and volume for prediction of aortic dissection, *Heart* 0 (2020) 1–6. doi:10.1136/heartjnl-2019-316251.
- [79] Y. Gal, Z. Ghahramani, Dropout as a bayesian approximation: Representing model uncertainty in deep learning, in: *Proc. of 33rd International Conference on Machine Learning (ICML)*, 2016.
- [80] I. Goodfellow, J. Pouget-Abadie, M. Mirza, et al., Generative adversarial nets, in: *Proc. of Advances in Neural Information Processing Systems*, Vol. 27, 2014, pp. 2672–2680.
- [81] K. Nazari, E. Ng, T. Joseph, et al., Edgeconnect: Generative image inpainting with adversarial edge learning, *CoRR abs/1901.00212*.
URL <http://arxiv.org/abs/1901.00212>
- [82] J. Wang, Y. Zhao, J. Noble, B. Dawant, Conditional generative adversarial networks for metal artifact reduction in ct images of the ear, in: *MICCAI: International Conference on Medical Image Computing and Computer-Assisted Intervention*, 2018, pp. 3–11. doi:10.1007/978-3-030-00928-1_1.
- [83] T. Miyato, T. Kataoka, M. Koyama, et al., Spectral normalization for generative adversarial networks, in: *Proc. of International Conference on Learning Representations*, 2018.
- [84] J. Johnson, A. Alahi, L. Fei-Fei, Perceptual losses for real-time style transfer and super-resolution, in: *Proc. of European Conference on Computer Vision*, 2016, pp. 694–711. doi:10.1007/978-3-319-46475-6_43.
- [85] G. Liu, F. A. Reda, K. J. Shih, et al., Image inpainting for irregular holes using partial convolutions, in: *Proc. of European Conference on Computer Vision*, 2018, pp. 89–105. doi:10.1007/978-3-030-01252-6_6.
- [86] A. Prutsch, A. Pepe, J. Egger, Design and development of a web-based tool for inpainting of dissected aortae in angiography images, in: *Proc. of Central European Seminar on Computer Graphics*, 2020.